

Flexible molecular-scale electronic devices

Sungjun Park, Gunuk Wang, Byungjin Cho, Yonghun Kim, Sunghoon Song, Yongsung Ji,

Myung-Han Yoon, and Takhee Lee

Table of Contents

1. Experiment

- 1.1. Fabrication of flexible molecular devices
- 1.2. Surface roughness of the PI substrate and bottom Au electrode
- 1.3. Cross-sectional images of bottom Au electrode under bending condition
- 1.4. Contact angle measurement of PEDOT:PSS on the SAM

2. Electrical transport under flat substrate condition

- 2.1. Conductance and resistance
- 2.2. Decay coefficient (β_N)
- 2.3. Comparison of R_{mol} with previous reported values
- 2.4. Stability of molecular electronic devices

3. Electrical transport under bending conditions

- 3.1. Electrical stability of Au/PEDOT:PSS/Au junctions
- 3.2. Resistance per molecule (R_{mol}) of the molecular junctions
- 3.3. J-V curves under different bending conditions
- 3.4. Decay coefficient (β_N) under bending conditions
- 3.5. Electrical and operational stability under gradual bending condition
- 3.6. Electrical and operational stability under bending condition
- 3.7. J-V characteristics under the extreme bending condition
- 3.8. J-V characteristics of twisted molecular junctions
- 3.9. Utilization of the other molecular components

4. Modelling: Stability of molecular junctions under bending condition

5. References

1. Experiment

1.1. Fabrication of flexible molecular devices

Figure S1 shows the fabrication scheme of our flexible molecular devices. First, patterned Au (500 Å)/Ti (100 Å) bottom electrodes were formed on the polyimide (PI) substrate using the shadow mask by an electron beam evaporator at a pressure of $\sim 10^{-7}$ torr and a deposition rate of ~ 0.2 Å/s (Fig. S1a). Photoresist (AZ5214) (~ 1.4 μm thick) was spin-coated on the patterned bottom electrodes to electrically isolate the molecular junctions (Fig. S1b). Holes in the photoresist layer were square-shaped and possessed side lengths ranging from 30 to 100 μm (increment of 10 μm). The devices were annealed in an oven at 470 K for 2 h to make the photoresist layer insoluble in ethanol during the formation of the molecular self-assembled monolayer (SAM) on the bottom electrode (Fig. S1c). After the molecular self-assembly process was performed, the devices were rinsed with ethanol to remove residual unbound molecules. To prevent electrical shorts in the molecular junctions, PEDOT:PSS (PH 1000 from CLEVIOS™, 700 S cm^{-1}) with 5% poly(3,4-ethylene-dioxythiophene) was spin-coated (~ 100 nm thick) on top of the SAM (Fig. S1d). To ensure good contact with hydrophobic SAM molecules, $\sim 1\%$ non-ionic surfactant (*t*-Oct-C₆H₄-(OCH₂CH₂)_xOH from Triton® X-100) was added to the PEDOT:PSS film prior to spin-coating. Au top electrodes (~ 500 nm thick) were deposited on top of the PEDOT:PSS layer using a shadow mask in an electron beam evaporator. The deposition conditions of the top Au electrodes were similar to those used to deposit the bottom electrodes (Fig. S1e). To prevent the formation of a direct current path through the PEDOT:PSS layer between the top and bottom Au electrodes, reactive ion etching (RIE) was performed with O₂ to remove redundant PEDOT:PSS layers on the devices. Figure S1f shows a schematic diagram and a real image of our flexible molecular devices.

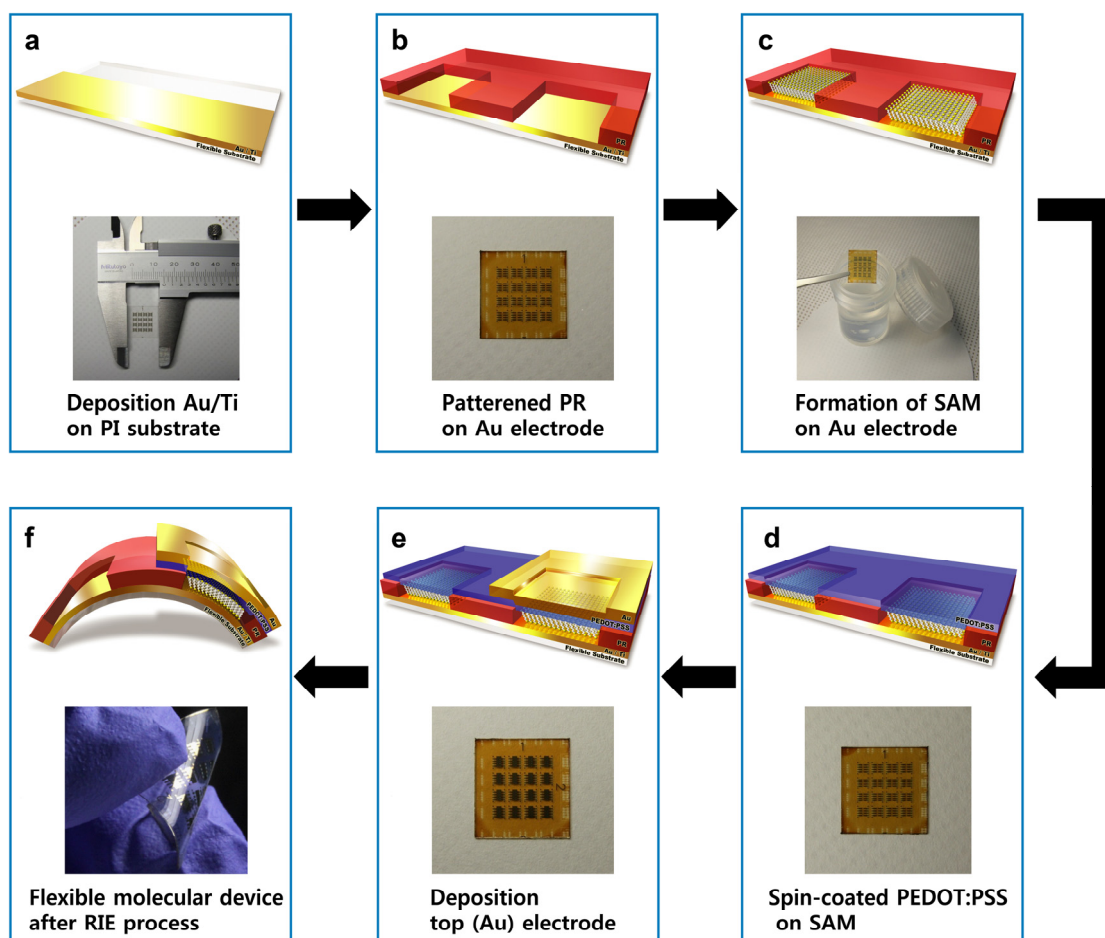


Figure S1. **a**, Patterning of Au/Ti bottom electrodes on the PI substrate using a shadow mask. **b**, Patterning of the photoresist layer. **c**, Formation of SAMs on Au electrodes. **d**, Spin-coating of the PEDOT:PSS layer. **e**, Deposition of Au top electrodes. **f**, Completed flexible molecular devices.

1.2. Surface roughness of the PI substrate and bottom Au electrode

As shown in Figure S2 and S3, PI substrate and Au electrode on PI substrate were measured using an atomic force microscope (XE-100, Park systems) and the RMS value of PI substrate and Au electrode before and after bending test were found as ~ 0.19 nm, 0.852 nm, and 0.893 nm from Figure S2, S3 (a) and S3 (b), respectively. In particular, there was no cracks observed on Au surface even after 1000 bending cycles (Figure S3 (b)).

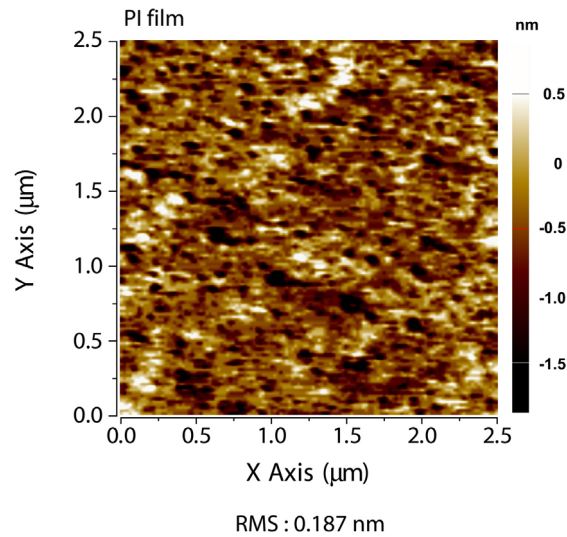


Figure S2. AFM image of the PI substrate.

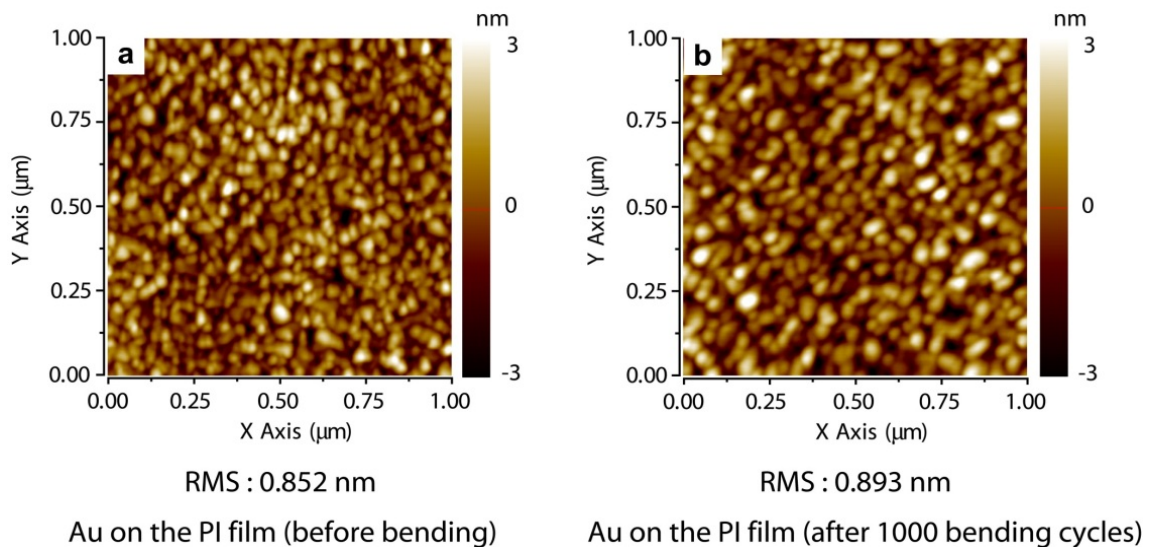


Figure S3. AFM images of the Au surface on PI substrate **a**, before and **b**, after the bending test of 1000 bending cycles.

1.3. Cross-sectional images of bottom Au electrode under bending condition

Figure S4 is the cross-sectional optical and field-emission scanning electron microscope (FESEM) images of the layers in small radius of bending curvature (bending radius: 5 mm). The images showed no delamination or adhesion problems after the bending test, also indicates that no significant changes occurred in the structure and phase of SAM molecules in the molecular junctions when the device was bent.

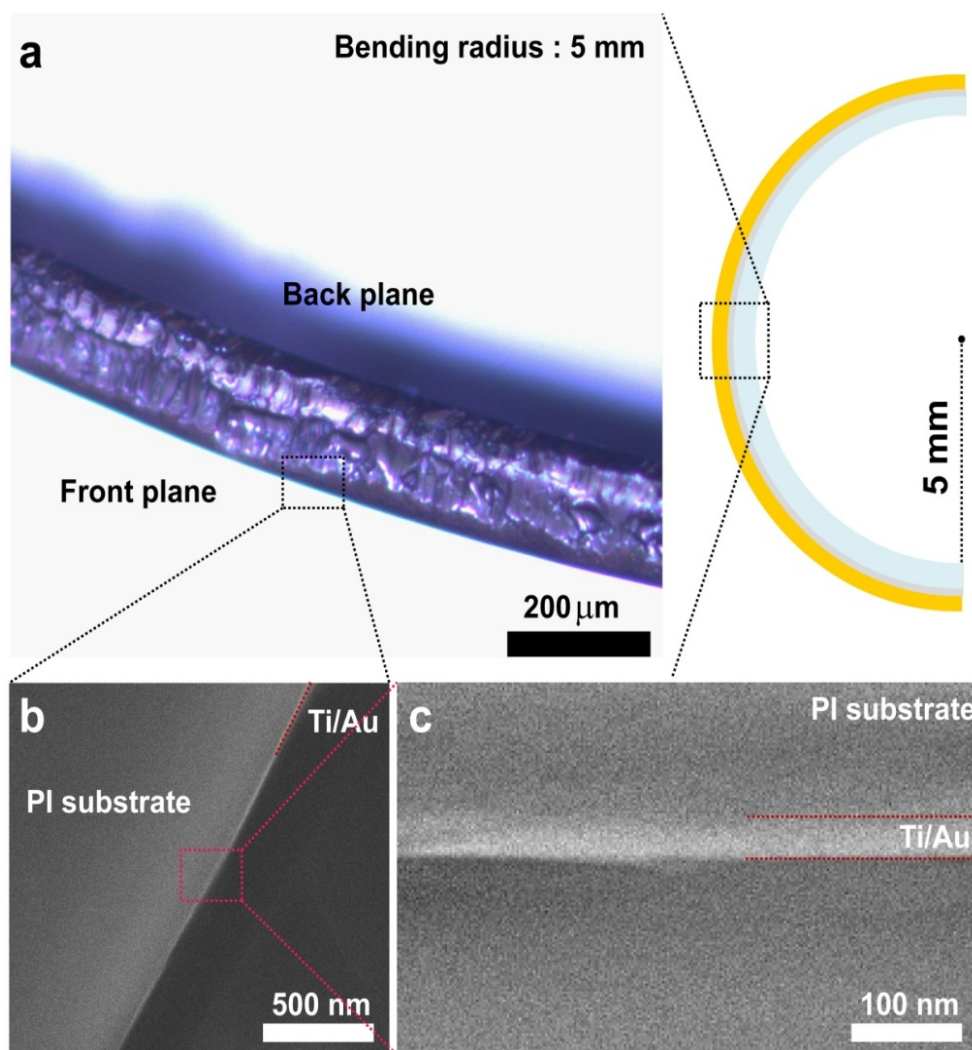


Figure S4. Cross-sectional **a**, optical image and **(b,c)** SEM images of Au/Ti layers on PI substrate under bent condition (bending radius: 5 mm). **b**, Low-magnification SEM image. **c**, High-magnification SEM image.

1.4. Contact angle measurement of PEDOT:PSS on the SAM

Figure S5 shows the contact angle measurement results of PEDOT:PSS on the C12 SAM. Contact angles as low as 20.9° were attained, indicating that the PEDOT:PSS film was in good contact with SAM molecules.

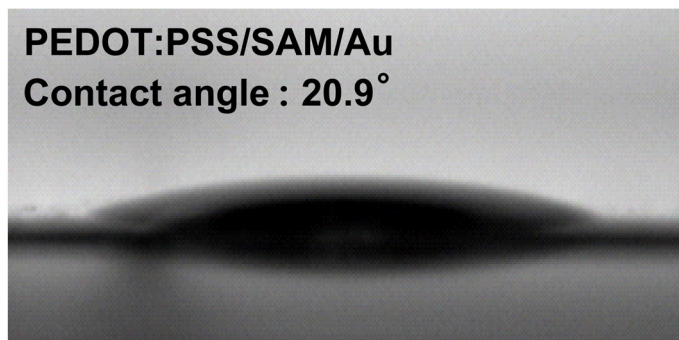


Figure S5. Contact angle of PEDOT:PSS on the C12 SAM.

2. Electrical transport under flat substrate condition

2.1. Au/PEDOT:PSS/molecule/Au, Au/PEDOT:PSS/Au, and Au/Au junctions

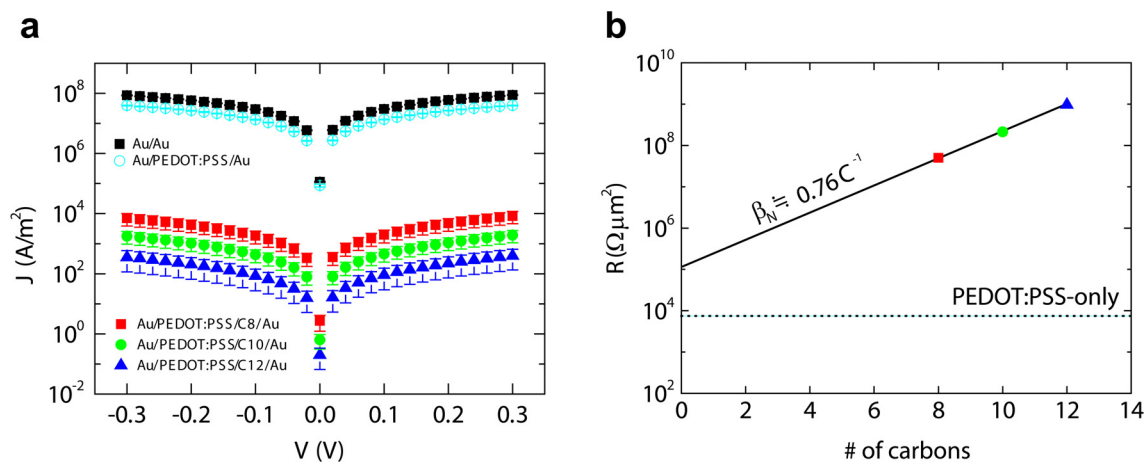


Figure S6. a, J-V data for Au/PEDOT:PSS/molecule/Au, Au/PEDOT:PSS/Au, and Au/Au junctions. **b**, The resistance as a function of the number of carbon atoms. The dotted line represents the resistance of Au/PEDOT:PSS/Au junctions.

2.2. Decay coefficient (β_N) under flat substrate conditions

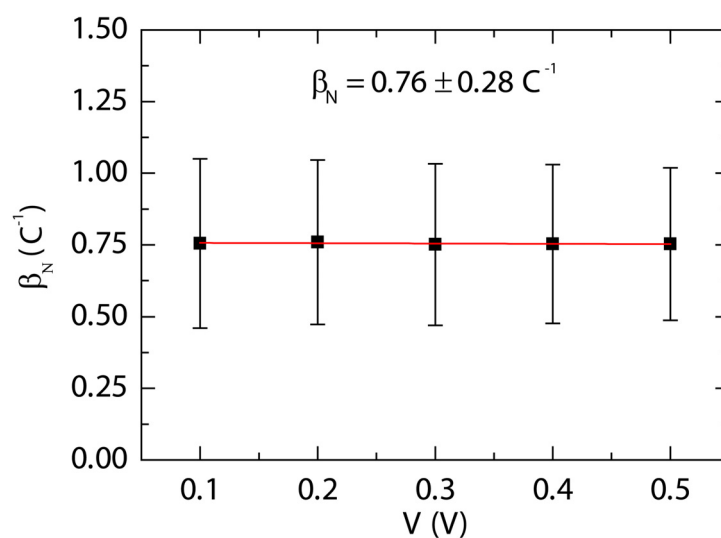


Figure S7. A plot of β_N vs. voltage for molecular junctions under flat substrate conditions. The β_N values were obtained from the linear fit of J-V data (inset of Fig. 1d in the main manuscript).

2.3. Comparison of R_{mol} with previous reported values

We compared our R_{mol} (the resistance per molecule) results to previous reported values for alkane-based molecular junctions, as summarized in Table S1. Specifically, we distinguished “single molecule measurement” type and “many molecules (bundle molecules) measurement” type^{S1-S14}.

Table S1. Transport parameters for alkane-based molecular junctions. Decay coefficient β and R_{mol} (the resistance per molecule) values are summarized.

| | Contacts | Technique | Number of molecules at the junctions | β (/C) | R_{mol} (M Ω) for C8 | R_{mol} (M Ω) for C12 | Ref. |
|---|---|---------------------|--|--------------|--------------------------------|---------------------------------|------|
| ■ | Au-S/SH-PEDOT | Polymer electrode | $3.2 \times 10^8 - 3.6 \times 10^{10}$ | 0.66 | $\sim 2 \times 10^6$ | $\sim 4 \times 10^7$ | S1 |
| | Au-S/CH ₃ -PmPV | Polymer electrode | $3.2 \times 10^8 - 3.6 \times 10^{10}$ | 1.13 | $\sim 8 \times 10^9$ | $\sim 8 \times 10^{12}$ | S2 |
| | Au-S/CH ₃ -Au | Au electrode | $\sim 1.5 \times 10^7$ | 1.08 | $\sim 2 \times 10^4$ | $\sim 2 \times 10^6$ | S3 |
| | Au-S/CH ₃ -Graphene | Graphene electrode | $\sim 1.5 \times 10^7$ | 1.06 | $\sim 7 \times 10^3$ | $\sim 4 \times 10^5$ | S4 |
| | Au-S/S-Hg | Hg-drop junction | $\sim 2.5 \times 10^{11}$ | 1.06 | - | - | S5 |
| | Au-S/CH ₃ -Au | Nanopores | 7300 | 0.83 | $\sim 2 \times 10^5$ | - | S6 |
| | Au-S/CH ₃ -Au | CP-AFM | 100-1000 | 0.88 | $\sim 4 \times 10^3$ | $\sim 1 \times 10^5$ | S7 |
| | Au-S/CH ₃ -Au | CP-AFM | 1000 | 1.01 | $\sim 4 \times 10^5$ | $\sim 1 \times 10^7$ | S8 |
| | Au-S/CH ₃ -Au-CH ₂ S-Au | Nanoparticle-bridge | 100 | 0.87 | - | - | S9 |
| □ | Au-S/S-Au | STM | 1 | 1.09 | $\sim 5.1 \times 10^1$ | - | S10 |
| | Au-S/S-Au | STM | 1 | 0.99 | $\sim 9.9 \times 10^2$ | - | S11 |
| | Au-S/S-Au | STM | 1 | 0.51 | $\sim 1.0 \times 10^3$ | - | S12 |
| | Au-S/S-Au | STM | 1 | 1.09 | $\sim 2.6 \times 10^2$ | - | S13 |
| | Au-S/S-Au | STM | 1 | 0.86 | $\sim 9.0 \times 10^2$ | - | S14 |

As shown in Figure S8, our R_{mol} values (symbol in red for C8, green for C10, and blue for C12) are in good agreement with the previous reported R_{mol} values of bundle molecules (red arrow for C8 and blue arrow for C12) obtained from the various measurement systems such as CP-AFM, break junctions, nanopore devices, microscale planar devices, and large area devices using conducting polymer (PEDOT:PSS and PmPV) or graphene electrodes.

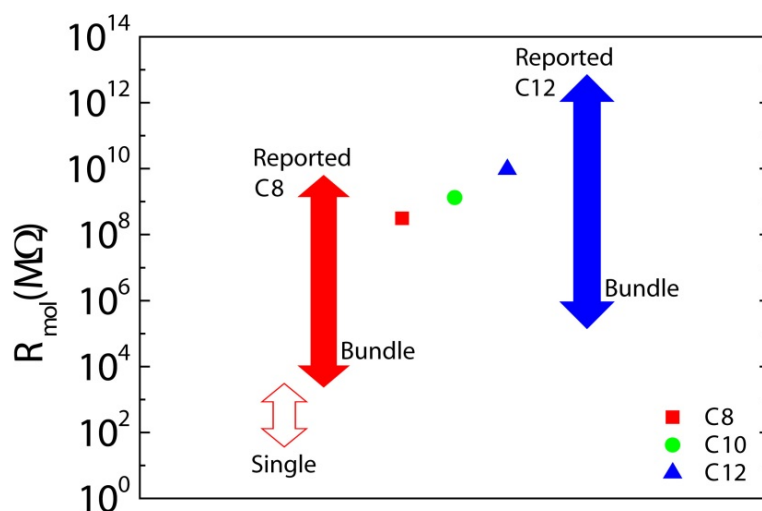


Figure S8. Comparison of R_{mol} (the resistance per molecule) values of our data (symbols) with previous reported values (arrows). Empty arrow represents the results for C8 molecule from scanning tunneling microscope (STM)-based single molecular junctions, and filled arrows represent the results of C8 and C12 molecules from various bundle molecular junctions.

2.4. Stability of molecular electronic devices

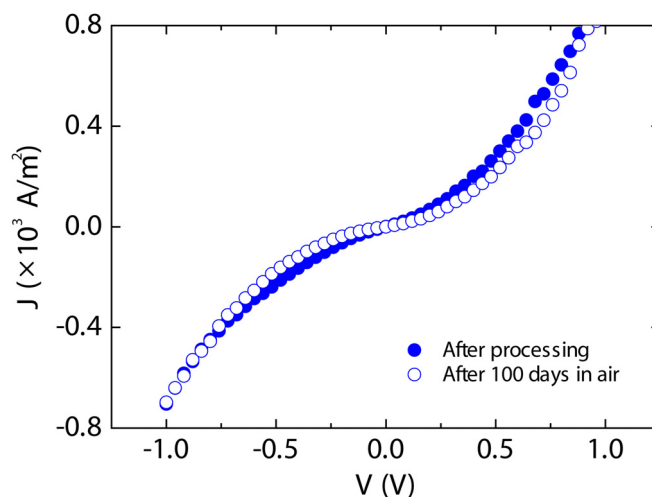


Figure S9. I-V characteristics for a C12 molecular junction immediately after device fabrication (filled circles) and after being stored for 100 days under ambient conditions (open circles).

3. Electrical transport under flat bending conditions

3.1. Electrical stability of Au/PEDOT:PSS/Au junctions under bending conditions

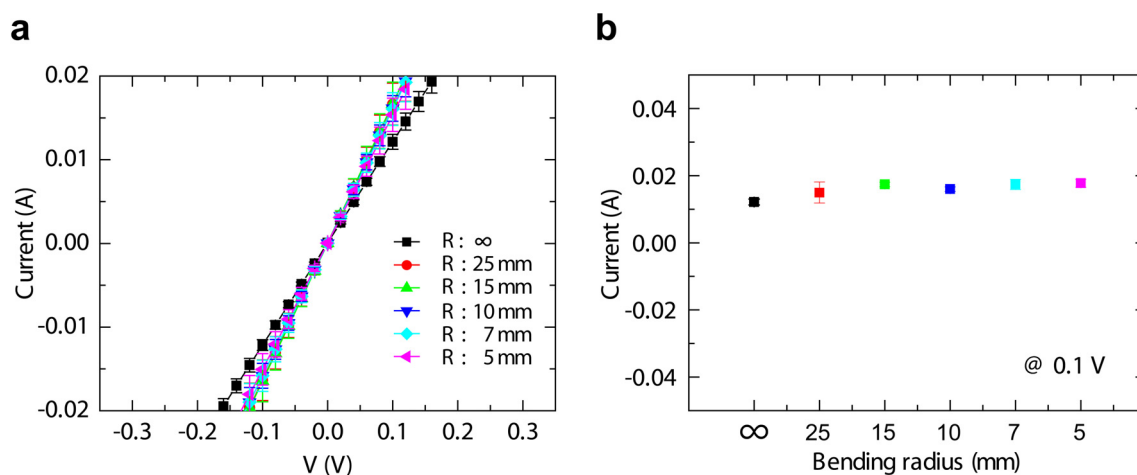


Figure S10. a, I-V data of Au/PEDOT:PSS/Au junctions for different bending radii (R). **b**, Currents measured at 0.1 V as a function of the bending radius.

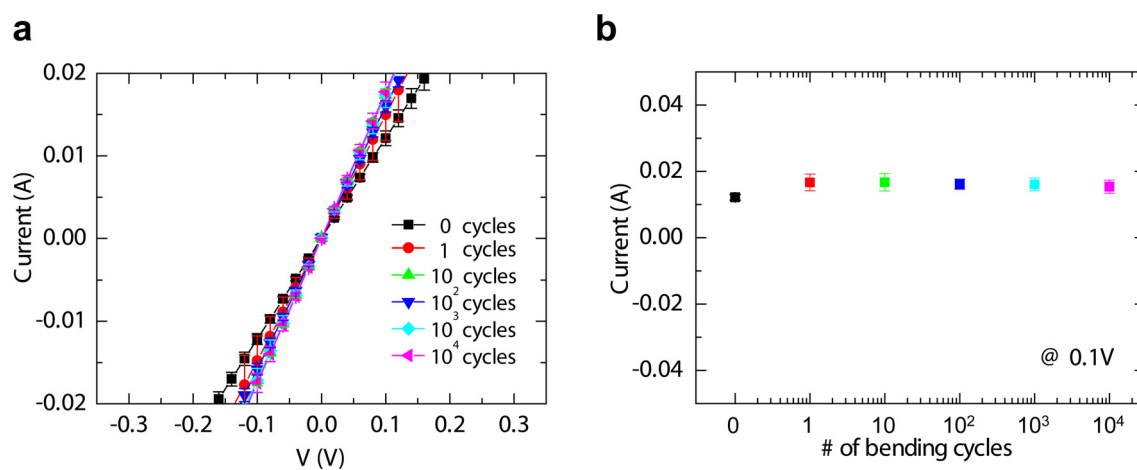


Figure S11. a, I-V data of Au/PEDOT:PSS/Au junctions under repeated bending cycles (up to 10⁴ cycles). **b**, Currents measured at 0.1 V as a function of the bending cycle.

3.2. Resistance per molecule (R_{mol}) of the molecular junctions

The resistance per molecule (R_{mol}) was obtained from the linear fit of each I-V curve at a low bias range ($-0.3 \leq V \leq 0.3$), and the grafting density ($4.6 \times 10^{18} /m^2$)^{S15} of alkanethiol molecules on Au(111) and the junction area were considered. R_{mol} values for C8, C10, and C12 flexible molecular devices under different bending conditions ($R = \infty$, 10 mm, and 5 mm) and in repeated bending cycles (0, 10^2 , and 10^3 times) are shown in Figures S12 and S13.

In the tables in Figures S12(c) and S13(c)), for example, the yield of 90% is not the yield of working devices after the device fabrication, instead it means the number of the stable devices after the bending test (Figure S12) or repetitive bending cycles (Figure S13).

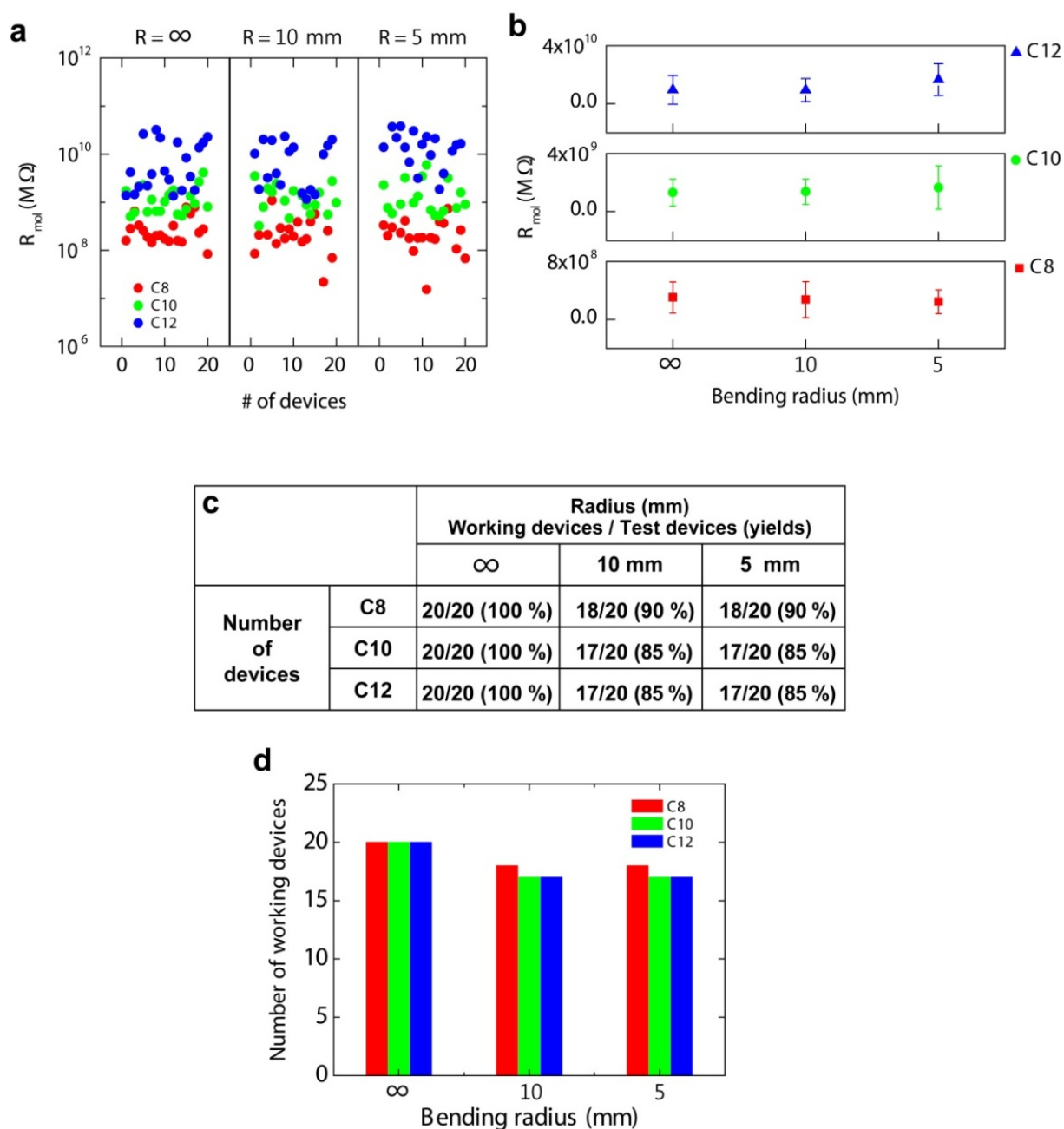


Figure S12. Statistical data of flexible molecular-scale devices. **a**, R_{mol} values for C8, C10, and C12 flexible molecular devices under different bending conditions ($R = \infty$, 10 mm, and 5 mm). **b**, A plot of the R_{mol} values under different bending radius conditions, which were obtained from the results in a. **(c,d)**, Table and histogram summarizing the statistics and device yields. For example, the number 18/20 means that 18 devices were stably working among the 20 tested devices under the given bending radius condition.

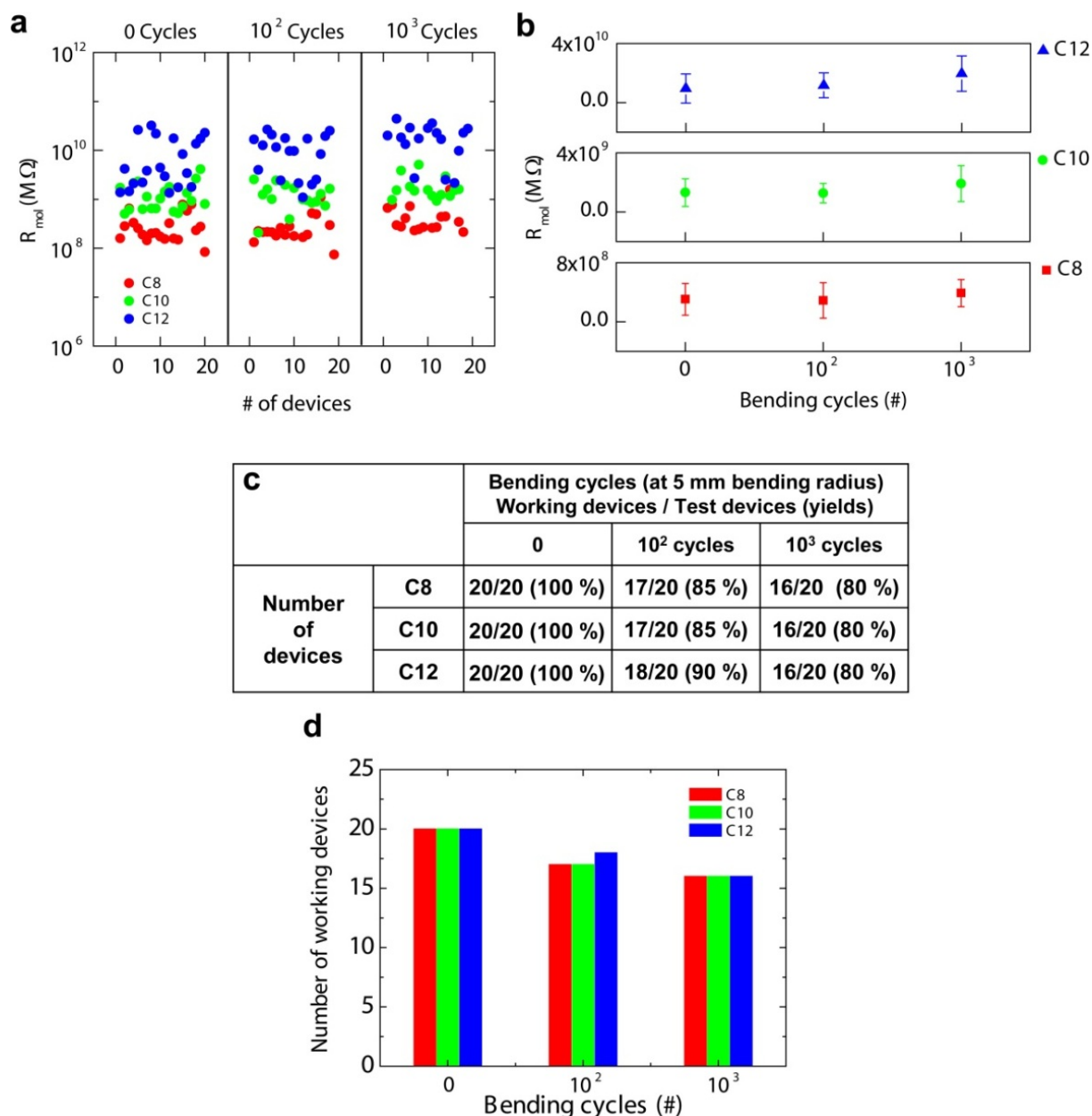


Figure S13. Statistical data of flexible molecular-scale devices. **a**, R_{mol} values for C8, C10, and C12 flexible molecular devices in repeated bending cycles (0, 10^2 , and 10^3 times). **b**, A plot of R_{mol} versus the bending cycle, which were obtained from the results in a. **(c,d)**, Table and histogram summarizing the statistics and device yields. For example, the number 17/20 means that 17 devices were stably working among the 20 tested devices under the given bending cycles.

3.3. *J-V* curves under different bending conditions

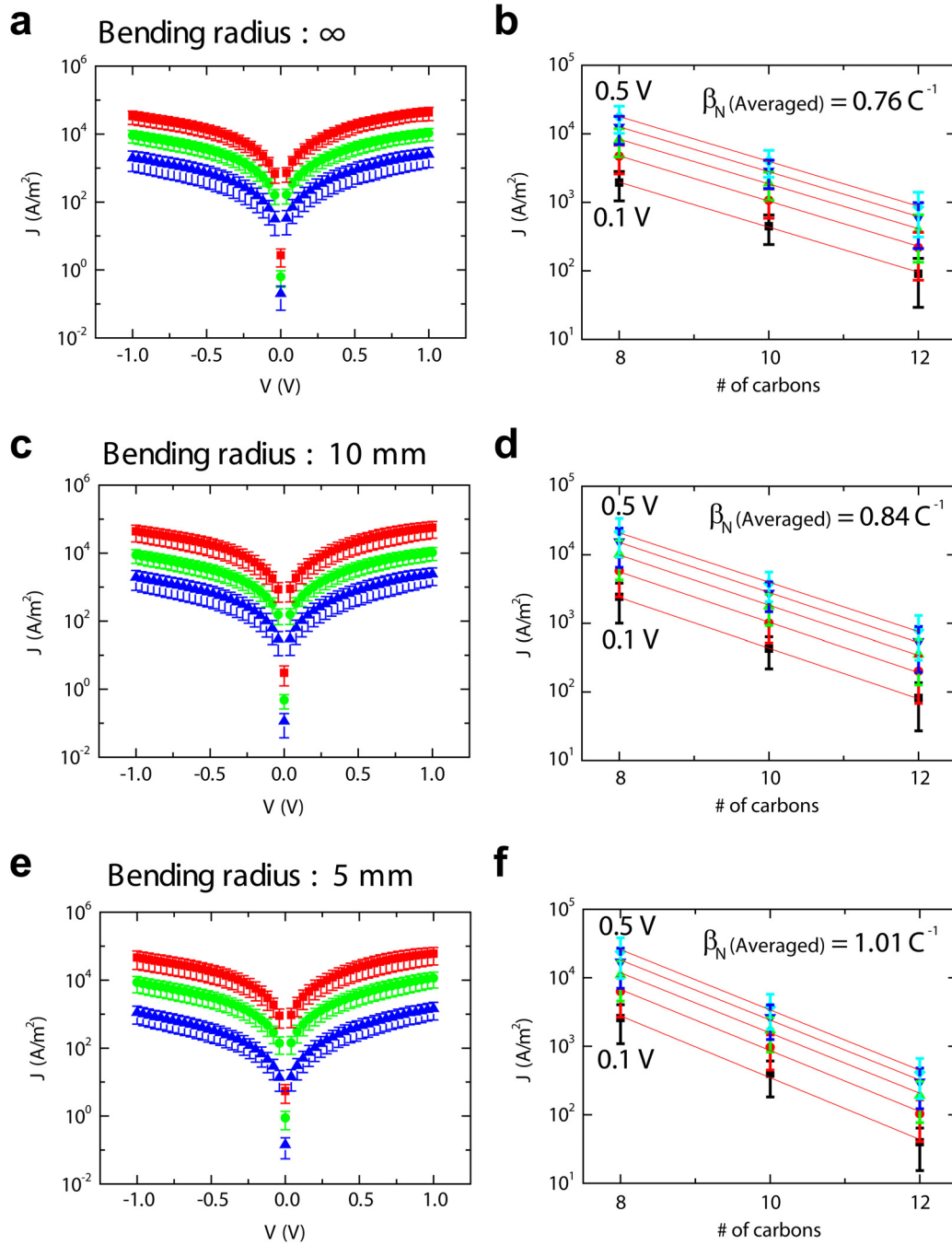


Figure S14. (a, c, e) Statistical J-V data for C8, C10, and C12 flexible molecular devices and (b, d, f) the molecular length dependence of currents with average decay coefficient (β_N) under different bending radii (a, b) $R = \infty$, (c, d) $R = 10 \text{ mm}$, and (e, f) $R = 5 \text{ mm}$.

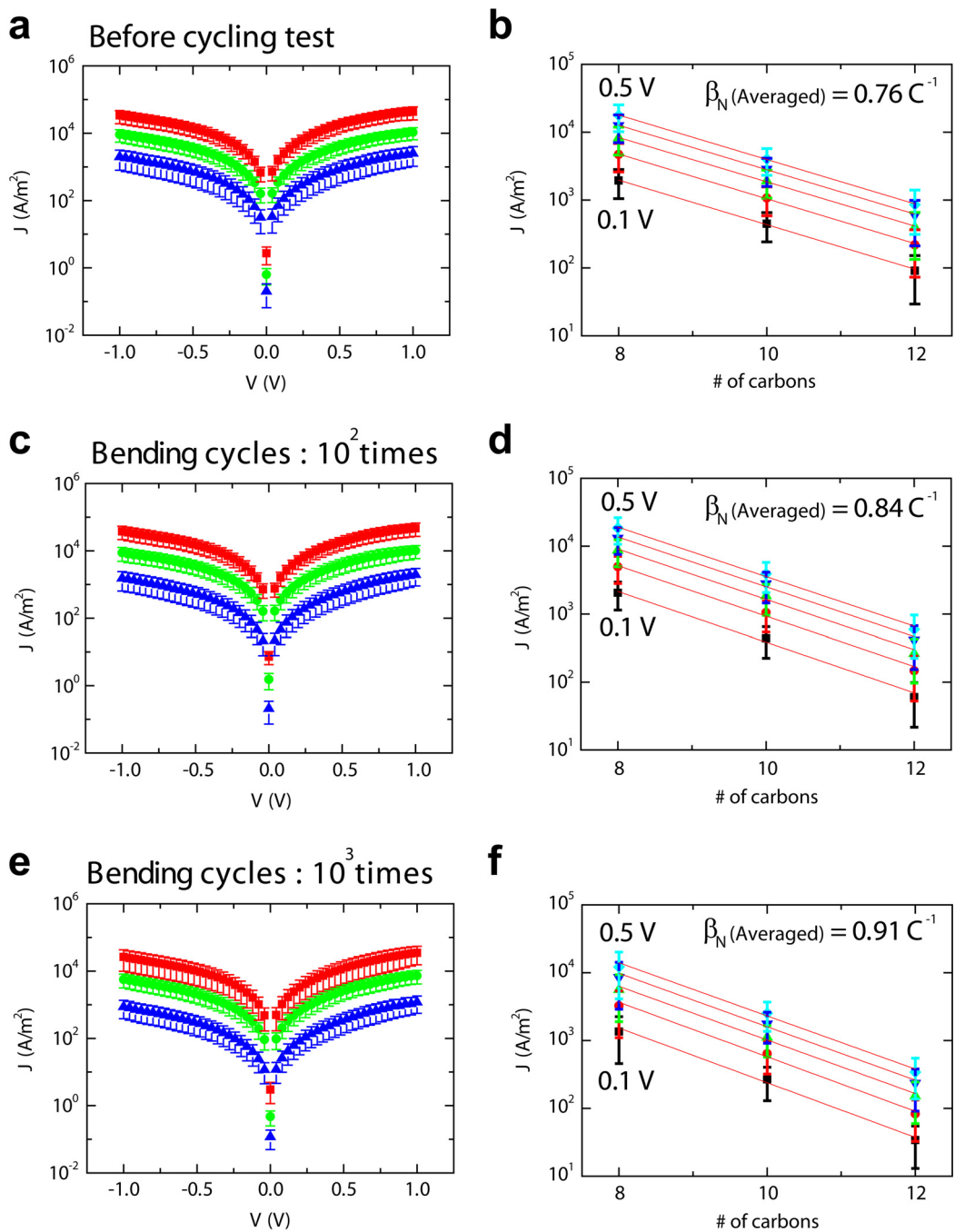


Figure S15. (a, c, e) Statistical J-V data for C8, C10, and C12 flexible molecular devices and (b, d, f) the molecular length dependence of currents with average decay coefficient (β_N) under repeated bending cycles: (a, b) 0 times (before the cycling test), (c, d) 10² times, and (e, f) 10³ times.

3.4. Decay coefficient (β_N) under bending

Figure S16 shows plots of the average decay coefficients under different bending conditions (bending radius and bending cycles), which were obtained from the results shown in Figs. S14 and S15. The decay coefficients increased slightly with an increase in bending (i.e., larger bending radius or more bending cycles). This phenomenon is an interesting topic that must be investigated further. Nevertheless, the observed β_N values were within the range of reported values for alkane-based molecules studied in different molecular junctions by other research groups (ranging from 0.51 to 1.13 C^{-1} , marked arrows in Fig. S19)^{S16}.

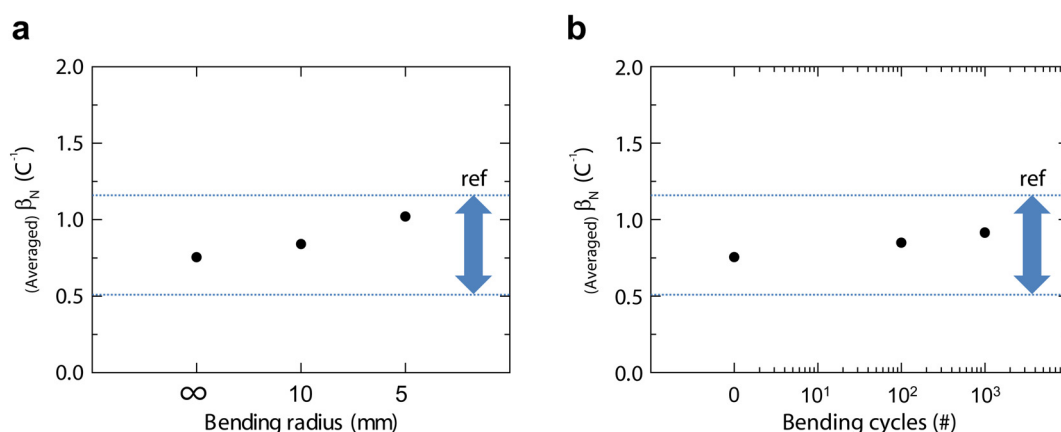


Figure S16. Decay coefficient (β_N) as a function of **a**, bending radius and **b**, bending cycle. Arrows indicate previously reported β_N values, which range from 0.51 to 1.13 C^{-1} .

3.5. Electrical and operational stability under gradual bending condition

To prove the operational stability of the flexible molecular devices, we performed J-V measurements under tensile and compressive bending conditions. C12 molecular devices on a PI substrate with dimensions of $15 \times 15 \text{ mm}^2$ were prepared and were characterised under different bending conditions. The fabricated device was bent incrementally with a vernier calliper, as explained in Fig. S17 and S18. The device was shaped into an arch by decreasing the width of the arc (d). In the arch shape, circles were drawn to fit the bent substrate (Fig. S17b and 18b), and the radius of curvature (r) was determined (Fig. S17c and S18c)^{S17}.

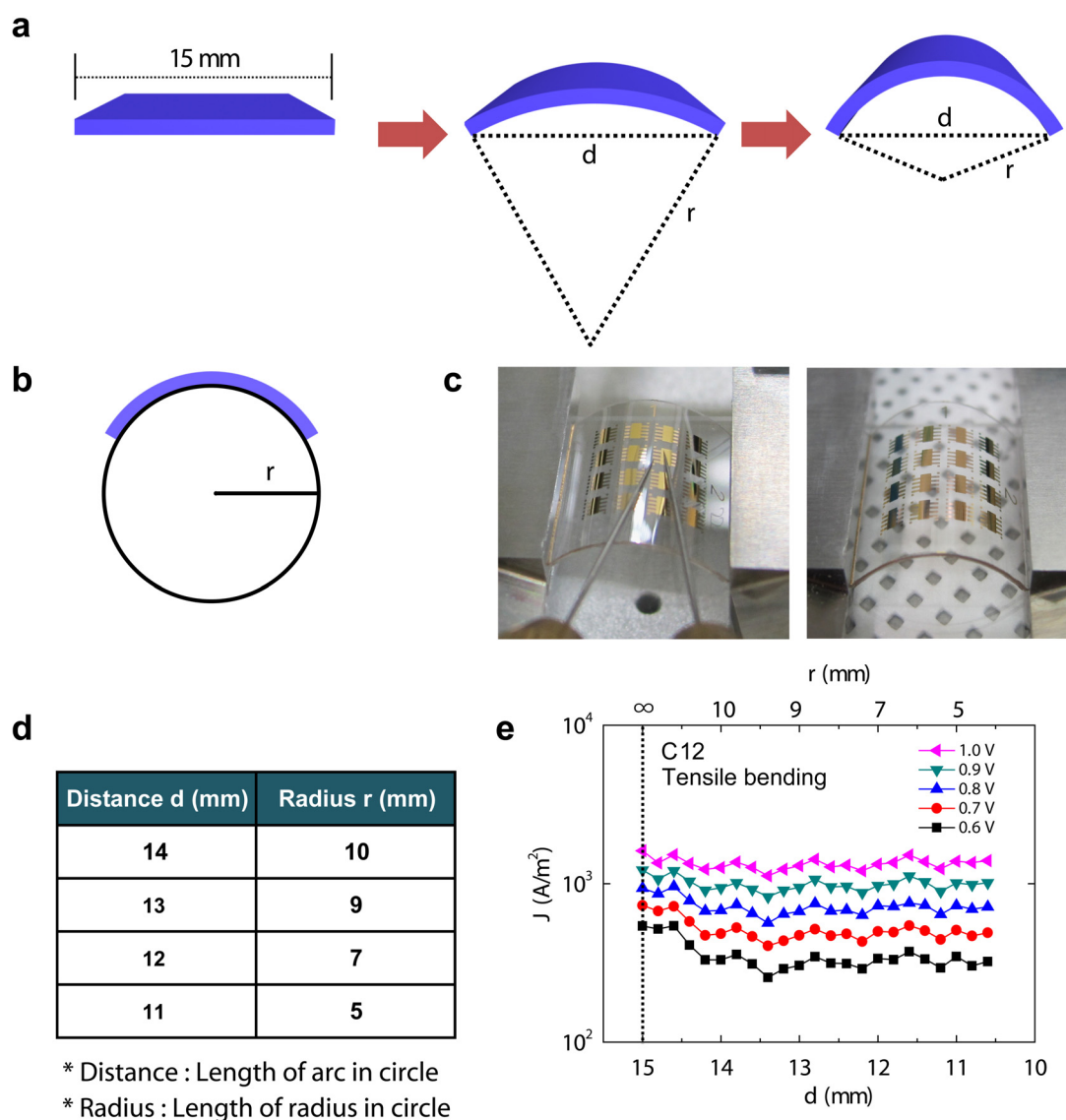
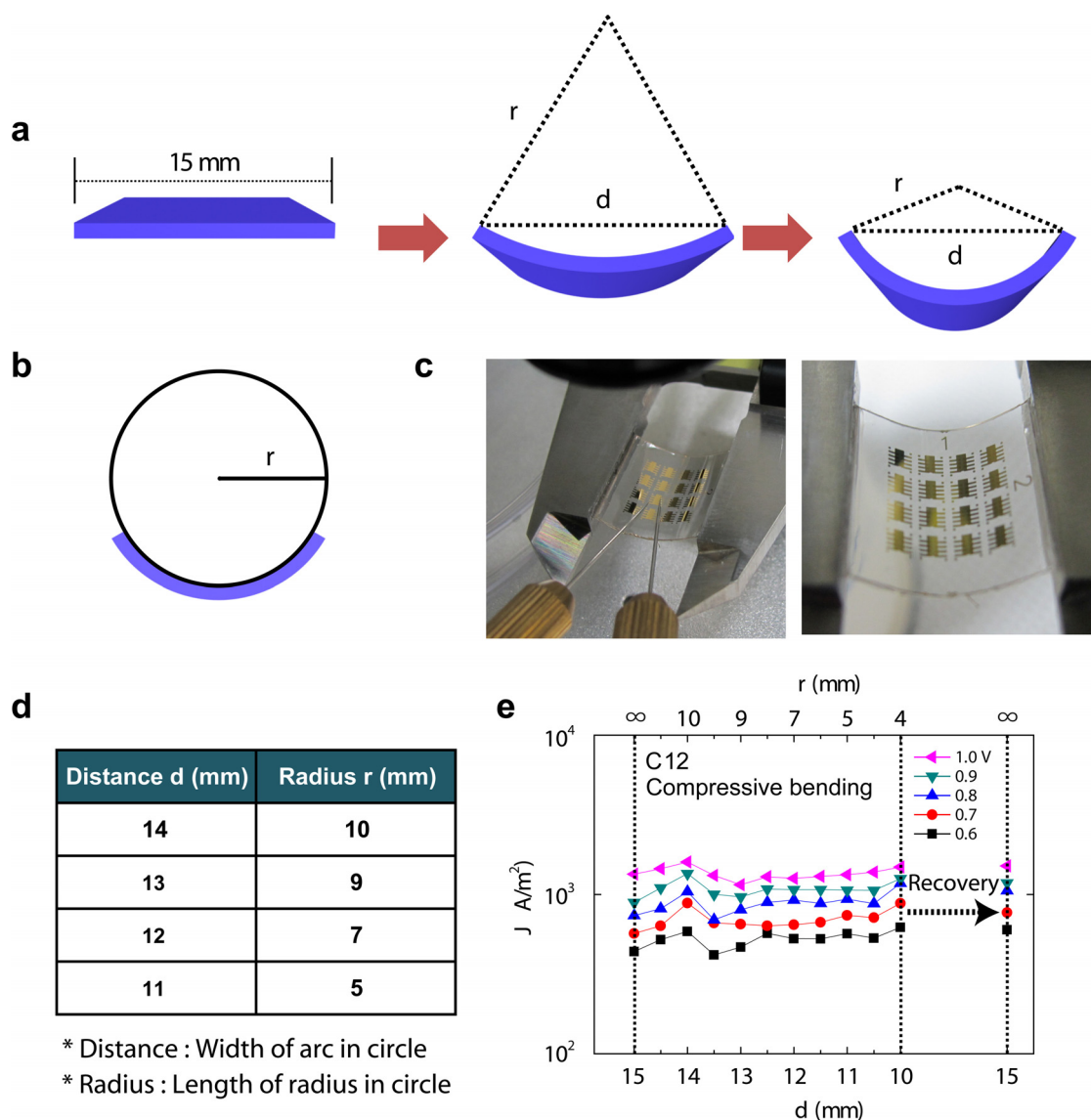


Figure S17. Flexible molecular-scale devices under tensile stress configuration. **(a,b)**, Schematic diagrams of the compressive substrate and the corresponding bending parameters (d and r). **c**, Photographic images of measuring molecular devices under compressive bending condition (tensile bending radius: 5 mm). **d**, A table lists the distance (d) and radius (r) used in this study. **e**, The J values of the C12 flexible device as a function of d and r (measured at voltages ranging from 0.6 to 1.0 V).



3.6. Electrical and operational stability under bending condition

The operation stability of our flexible molecular devices was investigated under different bending conditions. Figure S19a and b show the current density values obtained in retention tests conducted on a C12 molecular device under the tensile bending conditions measured at 0.8 V (Tensile bending radius of 5 mm for 10^4 s at $\Delta t = 100$ s) and the compressive bending conditions measured at 0.8 V and -0.8 V (Compressive bending radius of 5 mm for 5×10^3 s at $\Delta t = 10$ s) The results indicated that our flexible molecular devices were stable under various bending conditions.

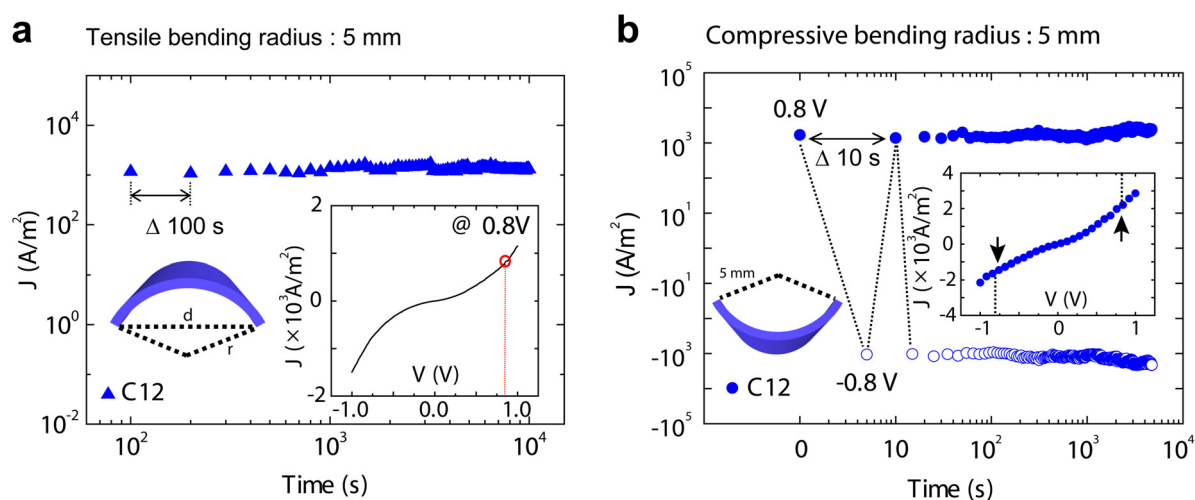


Figure S19. **a**, J values obtained during the retention test at 0.8 V for a C12 junction under bending conditions (Tensile bending radius = 5 mm). **b**, J values obtained during the retention test at ± 0.8 V for a C12 junction under bending conditions (Compressive bending radius = 5 mm).

3.7. Operation stability under the extreme bending condition

To prove that a tunnelling transport mechanism was relevant under bent conditions, we performed temperature variable J-V measurements on a C12 flexible molecular device on a toothpick (bending radius $\cong 1$ mm) (Figure S20a). As shown in Figure S20b, the J-V characteristics showed temperature-independent behaviour, which was indicative of tunnelling through a molecular barrier at temperatures ranging from 150-300 K.

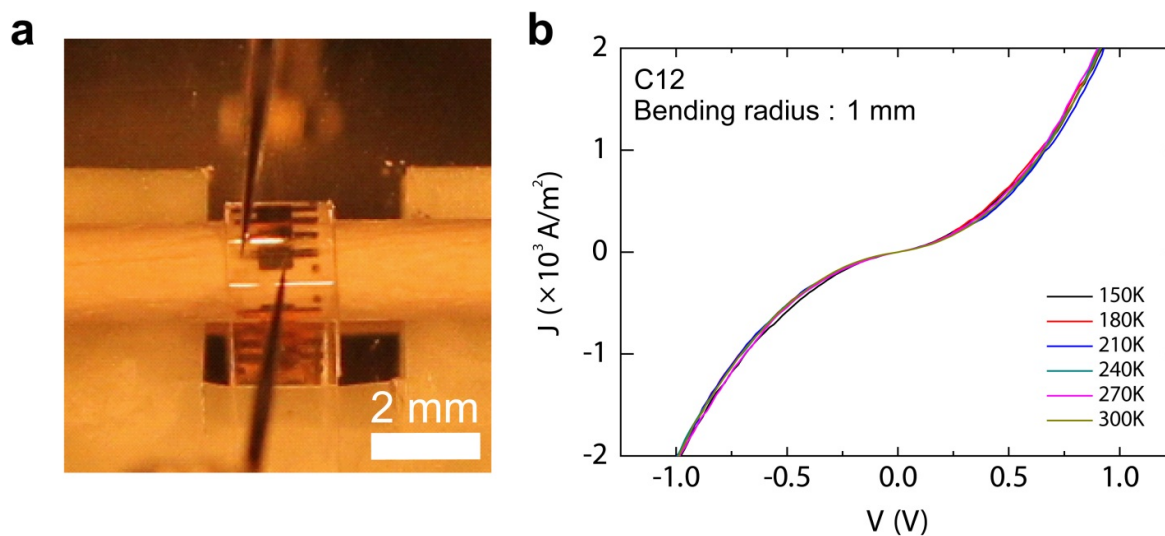


Figure S20. a, A photographic image of measuring temperature-variable transport properties of molecular devices under extreme bending condition in a cryostat chamber (compressive bending radius: 5 mm). **b,** J-V data for a C12 flexible device at different temperatures (from 150 to 300 K) under compressive bending conditions.

3.8. *J-V characteristics of twisted molecular junctions*

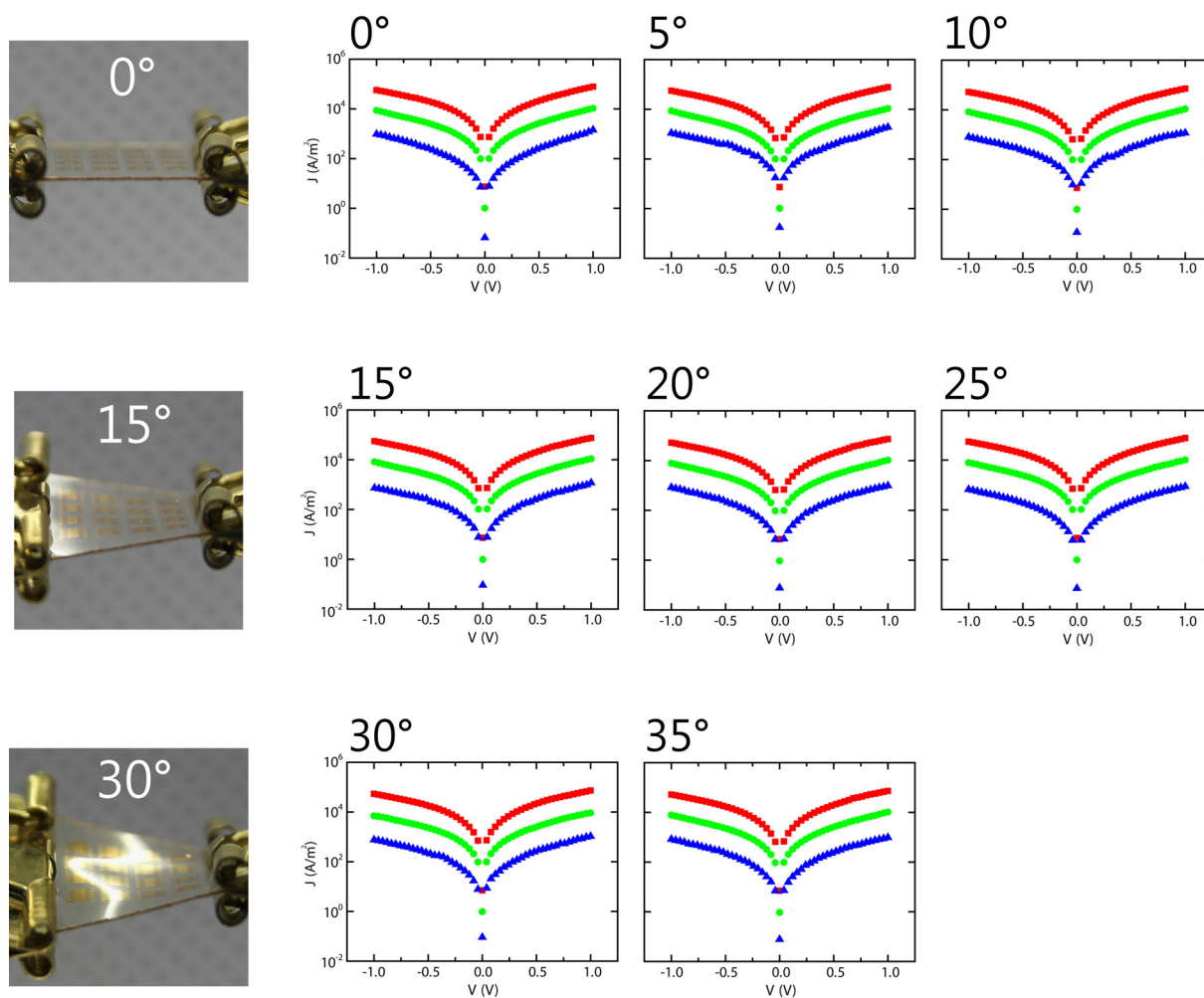


Figure S21. J-V characteristics of molecular junctions under twisted conditions.

3.9. Utilization of the other molecular components

As shown in Figure S22, different types of active molecules could also be applied on the plastic flexible substrate and retain their electrical properties under the bending conditions. The results with other molecular components are important to demonstrate that our approach of flexible molecular-scale devices can be applied to more other molecular kinds.

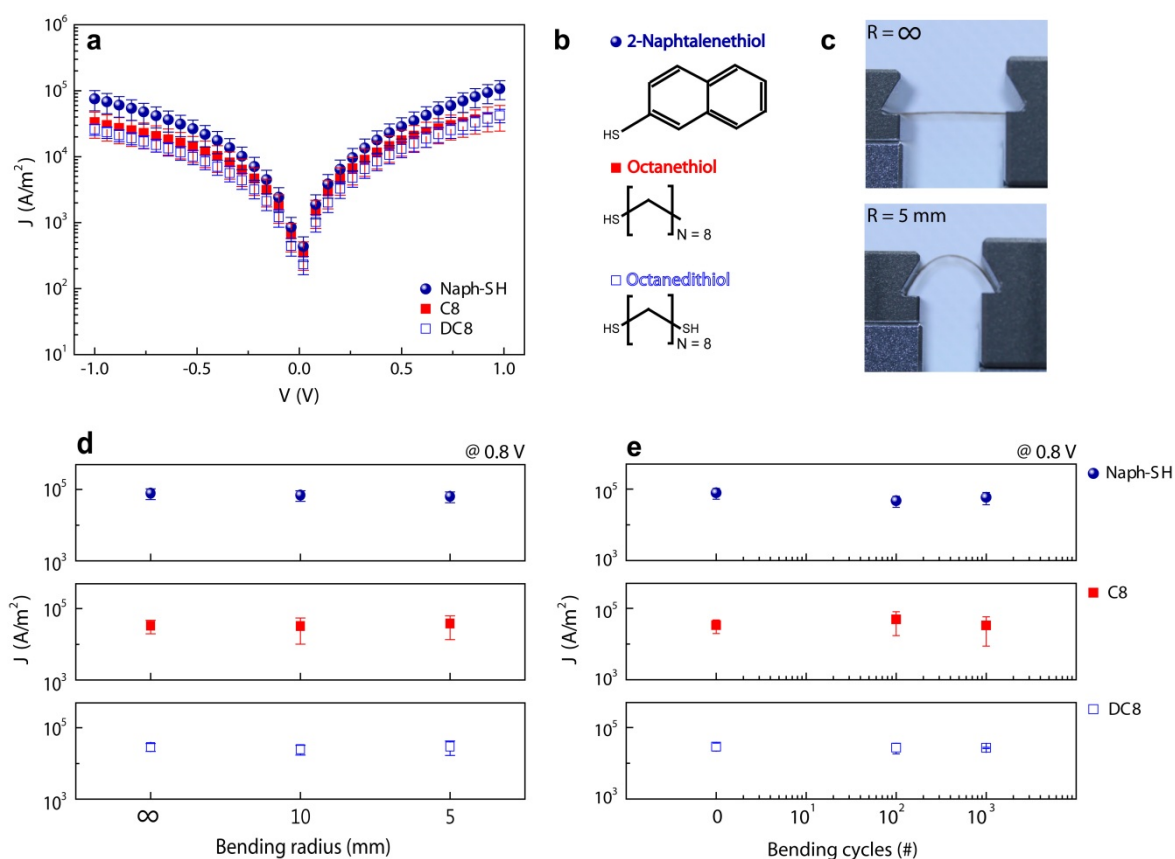


Figure S22. Statistical data of flexible molecular-scale devices with different molecular components. **a**, J-V curves for 2-Naphtalenethiol (denoted as Naph-SH), octanethiol (C8), and octanedithiol (DC8). The error bars represent the standard deviation of over 20 devices for each molecule. **b**, Three different types of molecular components. **c**, Flexible molecular devices under flat (top picture) and bending (bottom picture) state. **d**, J values of three types of molecular components measured at 0.8 V under different bending conditions ($R = \infty$, 10 mm, and 5 mm). **e**, J values of three types of molecular components measured at 0.8 V with repeated cycles.

4. Modelling: Stability of molecular junctions under bending condition

To explain the stable molecular device under bending condition, we analyzed the bending strain ε of SAM molecules on an Au/PI substrate. Figure S23a illustrates a sheet (SAM/Au/PI) bent with the bending radius of R . The SAM, Au, and PI in our molecular device have each thickness ($d_{\text{SAM}} \cong 1$ nm, $d_{\text{Au}} \cong 50$ nm, and $d_{\text{PI}} \cong 100$ μm) and Young's modulus ($Y_{\text{SAM}} \cong 0.28$ GPa (for C8), $Y_{\text{Au}} \cong 79$ GPa, and $Y_{\text{PI}} \cong 2.30$ GPa (for Neopulim L-3430))^{S22,S23}. When the sheet is bent, the top surface of sheet is in tension, which can be stretched by the bending strain ε_{top} ^{S20,S21}. The estimated bending strain ε_{top} for top film layer placed onto a substrate is given by the following equation,

$$\varepsilon_{\text{top}} = \left(\frac{d_f + d_s}{2R} \right) \frac{(1 + 2\eta + \chi\eta^2)}{(1 + \eta)(1 + \chi\eta)} \quad (\text{S1})$$

where $\eta = d_f/d_s$ (d_f and d_s are the thickness of the film layer and the substrate, respectively) and $\chi = Y_f/Y_s$ (Y_f and Y_s are the Young's modulus of the film layer and the substrate, respectively). In this equation, we can calculate the bending strain ε_{top} for Au (50 nm) and SAM/Au (1 nm/50 nm) sheet, as shown in Fig. S23b. Due to the thickness difference between Au and SAM layer ($d_{\text{Au}} \gg d_{\text{SAM}}$), the $\varepsilon_{\text{SAM/Au}}$ is similar to ε_{Au} when the R varies from 10 to 0.1 mm. Therefore, we can expect that $\varepsilon_{\text{SAM/Au/PI}} \cong \varepsilon_{\text{Au/PI}}$ in our bending condition ($R \geq 1$ mm).

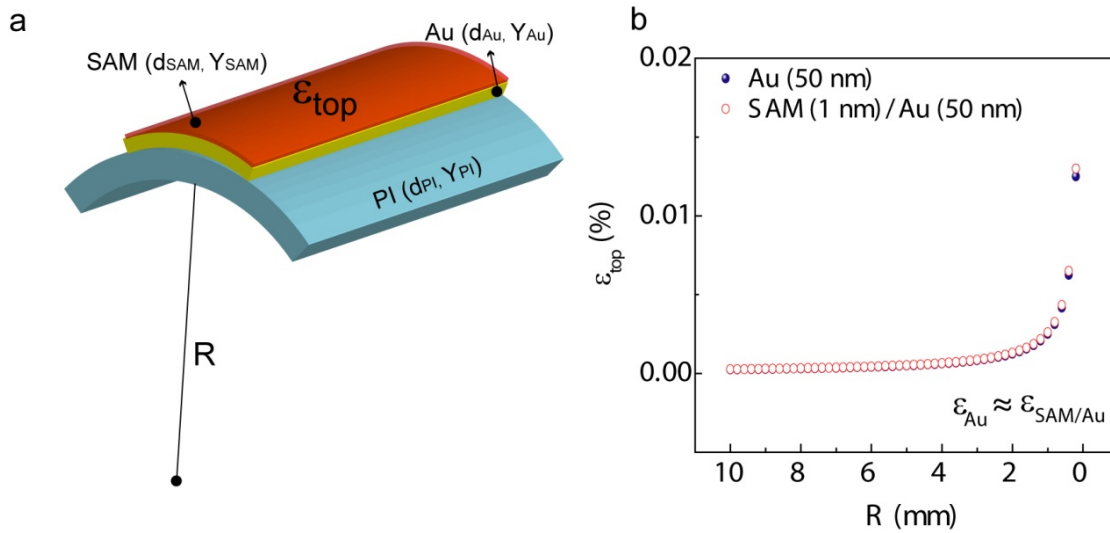


Figure S23. a, A SAM layer-on-Au/PI structure bends with a bending radius of R . **b**, A plot of the bending strain ϵ_{top} of top layer versus the bending radius R for the SAM/Au and Au substrates.

We can also estimate the bending strain ϵ_{top} of SAM on Au/PI structure as a function of the bending radius R and the thickness (d_{PI} and d_{Au}) of PI and Au. Figure S24 shows the contour plots of the ϵ_{top} of SAM on Au/PI structure as a function of the bending radius R (from 5 mm to 0.1 mm) and the thickness ($10 \mu\text{m} \leq d_{PI} \leq 1000 \mu\text{m}$ in increments of $10 \mu\text{m}$ and $1 \text{ nm} \leq d_{Au} \leq 100 \text{ nm}$ in increments of 1 nm) of PI and Au layer. As shown in Fig. S24a, the bending strain ϵ_{top} of SAM on Au/PI structure increases when the R decreases and the d_{PI} increases at the condition of $d_{Au} = 50 \text{ nm}$. However, as shown in Fig. S24b, this ϵ_{top} value is almost independent in the range of $d_{Au} \leq 100 \text{ nm}$ at the condition of $d_{PI} = 100 \mu\text{m}$. The black solid lines in Fig. S24 denote the $\epsilon_{top} = 12 \%$, which corresponds to the strain limit for non-cracking and electrical conducting of Au ($d_{Au} < 100 \text{ nm}$)^{S22,S23}, and the tensile elongation limit of PI substrate (Neopulim L-3430, MGC Co.). And, the white boxes in Fig. S24 denote the strain regions corresponding to the bending conditions applied to our devices ($1 \text{ mm} \leq R \leq 5 \text{ mm}$) and the thickness of PI and Au ($d_{PI} = 100 \mu\text{m}$ and $d_{Au} = 50 \text{ nm}$). In the bending tests of our flexible molecular devices, the bending radius R was varied from ∞ to 1 mm ,

corresponding to the bending strain ϵ_{top} from 0 % to 4.92 %. Therefore, it can be expected that the top surface of Au/PI substrate might be stretched by $\epsilon_{\text{top}} = 4.92$ % at $R = 1$ mm.

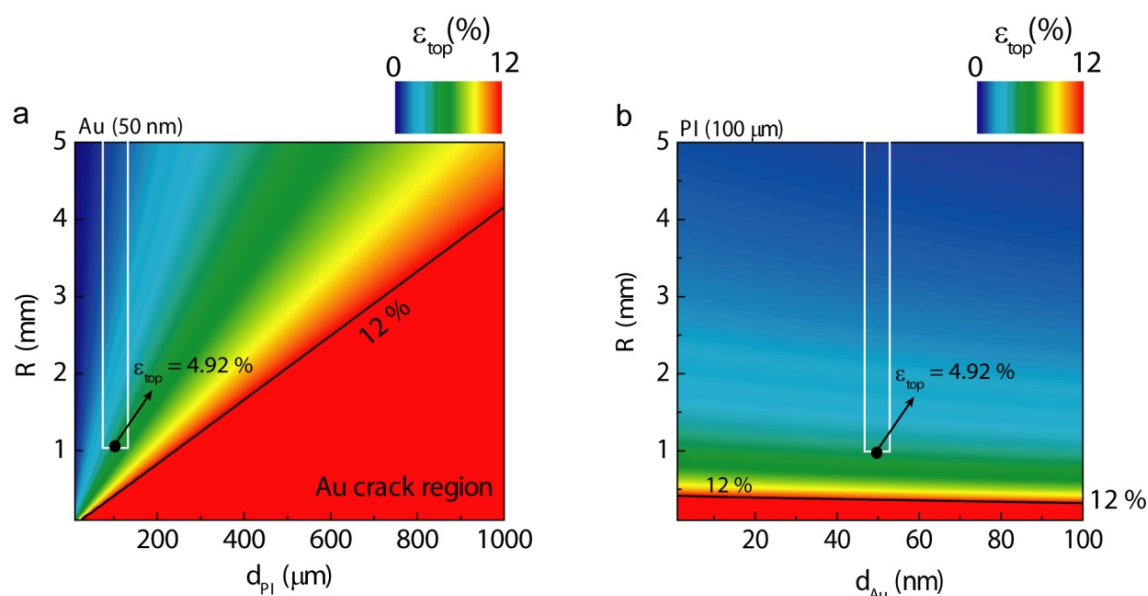


Figure S24. a, Contour plot of the bending strain ϵ_{top} of SAM on Au/PI as a function of the bending radius R and the thickness d_{PI} at a fixed $d_{\text{Au}} = 50$ nm. **b**, Contour plot of the bending strain ϵ_{top} of SAM on Au/PI as a function of the bending radius R and the thickness d_{Au} at a fixed $d_{\text{PI}} = 100 \mu\text{m}$. The black solid lines correspond to the $\epsilon_{\text{top}} = 12$ %. The white boxes correspond to the bending and device structure condition in our study ($1 \text{ mm} \leq R \leq 5 \text{ mm}$, $d_{\text{PI}} = 100 \mu\text{m}$, and $d_{\text{Au}} = 50 \text{ nm}$).

To estimate the amount of current change in the molecular junction under bending conditions, we consider the model of two transport tunnelling pathways in alkanemonothiol molecular junction^{S20,S21}. One is the “Through-Bond” (TB) pathway and the other is the “Through-Space” (TS) (so called the chain-to-chain transport) pathway (Fig. S25). In the case of TB tunnelling, charge flows along the σ -bond in the backbone of the alkyl chains. In contrast, TS tunnelling involves lateral hops via intermolecular couplings between neighbouring alkyl chains. Therefore, the total tunnelling current I_{total} through the SAM based on these pathways is given by^{S20},

$$I_{total} = I_{TB} + I_{TS} \propto e^{(-\beta_{TB} \times d_{SAM})} + e^{(-\beta_{TB} \times (d_{SAM} - d_{cc} \tan \theta))} e^{(-\beta_{TS} \times d_{cc})} \quad (S2)$$

where β_{TB} is the decay coefficient for TB tunnelling ($\beta_{TB} = 0.61 \text{ \AA}^{-1}$ in the PEDOT:PSS-interlayer molecular junction case), β_{TS} is the decay coefficient for TS tunnelling ($\beta_{TS} = 1.31 \text{ \AA}^{-1}$)^{S15}, d_{SAM} is molecular length, θ is the molecular tilt angle with respect to the Au surface normal, and d_{cc} is the chain-to-chain distance ($\sim 4.98 \text{ \AA}$)^{S20}. When the molecular device is bent with a bending radius R , the top side of junction structure can be stretched by the bending strain ϵ_{top} , which leads to the change in length ΔL per unit of the original length L of the Au bottom electrode (Fig. S25a). In this result, the original distance d_{cc} between molecular chains can be changed to the $d_{cc} + \Delta d_{cc}$, which leads to the change in TS tunnelling pathway (Fig. S25a). However, the molecular length d_{SAM} does not change in a bent condition, which leads to no difference of TB tunnelling pathway between flat and bent condition. Therefore, the total tunnelling current in a bent condition can be given by

$$I_{total} \propto e^{(-\beta_{TB} \times d_{SAM})} + e^{(-\beta_{TB} \times (d_{SAM} - (d_{cc} + \Delta d_{cc}) \tan \theta))} e^{(-\beta_{TS} \times (d_{cc} + \Delta d_{cc}))} \quad (S3)$$

From the Eq. (S2) and (S3), we can estimate the total current change (i.e., $\Delta I_{total}/I_{total}$) where ΔI_{total} is the tunnelling current difference between a flat and a bent condition, and I_{total} is the tunnelling current in a flat condition). Figure S25b shows the change in tunnelling current of the molecular device as a function of the bending radius R . When the bending radius R varies from 10 mm to 1 mm, the change in total current of molecular device is negligible (for example, $\Delta I_{total}/I_{total}$ was found to be ~ 0.0017 at bending radius $R = 1 \text{ mm}$ condition). This is because the charge conduction by the TS tunnelling pathway is negligible as compared with the dominant TB tunnelling in the overall charge transport. From this result, we can explain the stability of flexible molecular-scale device under the deformed conditions.

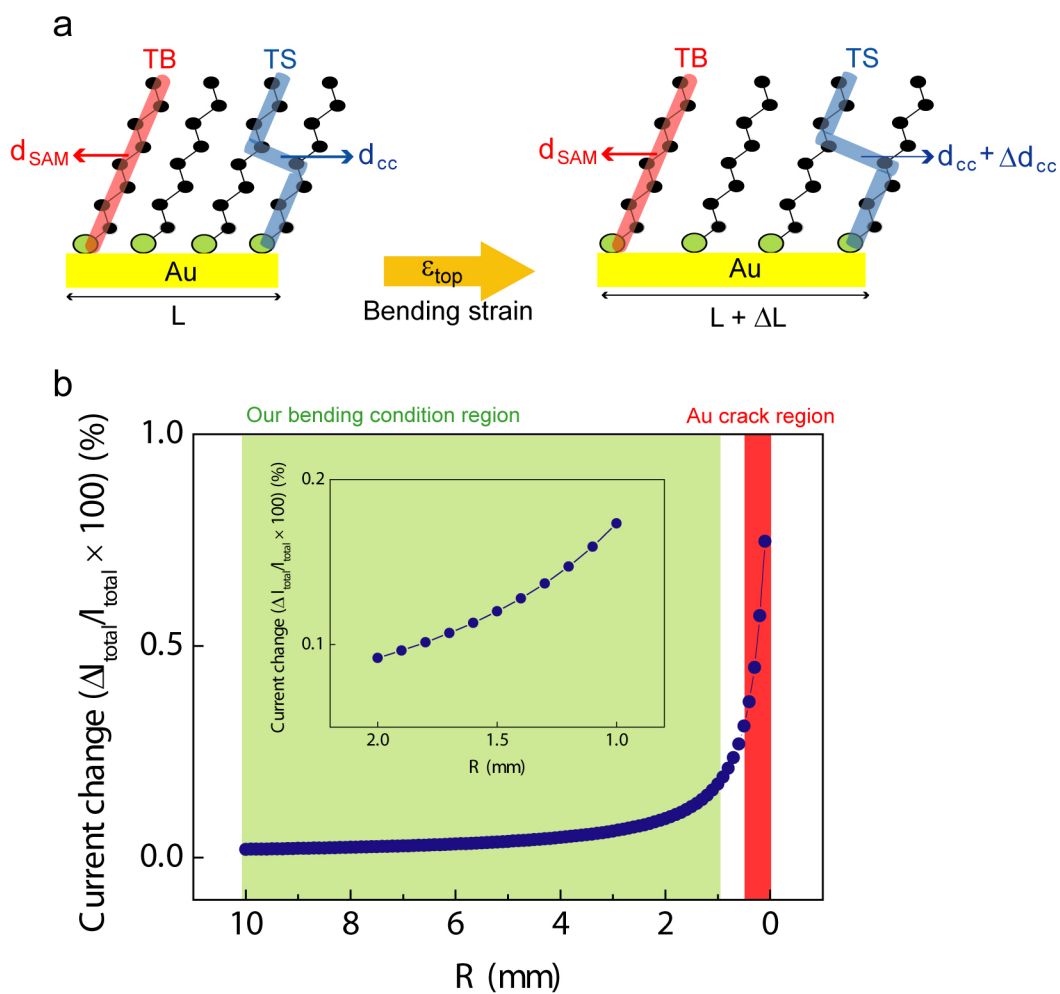


Figure S25. a, Schematic illustrating tunnelling pathways (through-bond (TB) and through-space (TS)) through molecular layer in a flat (left side) and a bent (right side) condition. **b**, A plot of the amount of the current change in molecular junction ($\Delta I_{total}/I_{total}$) as a function of the bending radius R . Inset is a zoomed-in plot showing the current change under bending radius R from 2 to 1 mm.

5. References

- S1. Akkerman, H. B. et al. Self-assembled-monolayer formation of long alkanedithiols in molecular junctions. *Small* **4**, 100-104 (2008).
- S2. Milani, F., Grave, C., Ferri, V., Samori, P. & Rampi, M. A. Ultrathin pi-conjugated polymer films for simple fabrication of large-area molecular junctions. *Chemphyschem* **8**, 515-518 (2007).
- S3. Kim, T. W., Wang, G. N., Lee, H. & Lee, T. Statistical analysis of electronic properties of alkanethiols in metal-molecule-metal junctions. *Nanotechnology* **18** 315204 (2007).
- S4. Wang, G., Kim, Y., Choe, M., Kim, T. W. & Lee, T. A New Approach for Molecular Electronic Junctions with a Multilayer Graphene Electrode. *Adv. Mater.* **23**, 755-760 (2011).
- S5. York, R. L., Nguyen, P. T. & Slowinski, K. Long-range electron transfer through monolayers and bilayers of alkanethiols in electrochemically controlled Hg-Hg tunneling junctions. *J. Am. Chem. Soc.* **125**, 5948-5953 (2003).
- S6. Wang, W. Y., Lee, T. & Reed, M. A. Mechanism of electron conduction in self-assembled alkanethiol monolayer devices. *Phys. Rev. B* **68**, 035416 (2003).
- S7. Engelkes, V. B., Beebe, J. M. & Frisbie, C. D. Length-dependent transport in molecular junctions based on SAMs of alkanethiols and alkanedithiols: Effect of metal work function and applied bias on tunneling efficiency and contact resistance. *J. Am. Chem. Soc.* **126**, 14287-14296 (2004).
- S8. Beebe, J. M., Engelkes, V. B., Miller, L. L. & Frisbie, C. D. Contact resistance in metal-molecule-metal junctions based on aliphatic SAMs: Effects of surface linker and metal work function. *J. Am. Chem. Soc.* **124**, 11268-11269 (2002).
- S9. Chu, C. W., Na, J. S. & Parsons, G. N. Conductivity in alkylamine/gold and alkanethiol/gold molecular junctions measured in molecule/nanoparticle/molecule bridges and conducting probe structures. *J. Am. Chem. Soc.* **129**, 2287-2296 (2007).
- S10. Xu, B. Q. & Tao, N. J. J. Measurement of single-molecule resistance by repeated formation of molecular junctions. *Science* **301**, 1221-1223 (2003).
- S11. Suzuki, M., Fujii, S. & Fujihira, M. Measurements of currents through single

- molecules of alkanedithiols by repeated formation of break junction in scanning tunneling microscopy under ultrahigh vacuum. *Jpn. J. Appl. Phys.* **45**, 2041-2044 (2006).
- S12. Haiss, W. *et al.* Measurement of single molecule conductivity using the spontaneous formation of molecular wires. *Phys. Chem. Chem. Phys.* **6**, 4330-4337 (2004).
- S13. Chen, F., Li, X. L., Hihath, J., Huang, Z. F. & Tao, N. J. Effect of anchoring groups on single-molecule conductance: Comparative study of thiol-, amine-, and carboxylic-acid-terminated molecules. *J. Am. Chem. Soc.* **128**, 15874-15881 (2006).
- S14. Cui, X. D. *et al.* Reproducible measurement of single-molecule conductivity. *Science* **294**, 571-574 (2001).
- S15. Seo, K. & Lee, H. Molecular electron transport changes upon structural phase transitions in alkanethiol molecular junctions. *ACS Nano* **3**, 2469-2476 (2009).
- S16. Akkerman, H. B. & de Boer, B. Electrical conduction through single molecules and self-assembled monolayers. *J. Phys. Condens. Matter.* **20**, 013001 (2008).
- S17. Ji, Y., Lee, S., Cho, B., Song, S. & Lee, T. Flexible organic memory devices with multilayer graphene electrodes. *ACS Nano* **5**, 5995-6000 (2011).
- S18. DelRio, F. W., Jaye, C., Fischer, D. A. & Cook, R. F. Elastic and adhesive properties of alkanethiol self-assembled monolayers on gold. *Appl. Phys. Lett.* **94**, 131909 (2009).
- S19. Kim, K. S., Song, J. Y., Chung, E. K., Park, J. K. & Hong, S. H. Relationship between mechanical properties and microstructure of ultra-fine gold bonding wires. *Mech. Mater.* **38**, 119-127 (2006).
- S20. Suo, Z., Ma, E. Y., Gleskova, H. & Wagner, S. Mechanics of rollable and foldable film-on-foil electronics. *Appl. Phys. Lett.* **74**, 1177-1179 (1999).
- S21. Song, K. *et al.* Fully Flexible solution-deposited ZnO thin-film transistors. *Adv. Mater.* **22**, 4308 (2010).
- S22. Lacour, S. P., Wagner, S., Huang, Z. Y. & Suo, Z. Stretchable gold conductors on elastomeric substrates. *Appl. Phys. Lett.* **82**, 2404-2406 (2003).
- S23. Lacour, S. P., Huang, Z. Y., Suo, Z. & Wagner, S. Deformable interconnects for conformal integrated circuits. *Mat. Res. Soc. Symp. Proc.* **736**, D4.8.1 (2003).
- S24. Yamamoto, H. & Waldeck, D. H. Effect of tilt-angle on electron tunneling through

- organic monolayer films. *J. Phys. Chem. B* **106**, 7469-7473 (2002).
- S25. Slowinski, K., Chamberlain, R. V., Miller, C. J. & Majda, M. Through-bond and chain-to-chain coupling. Two pathways in electron tunneling through liquid alkanethiol monolayers on mercury electrodes. *J. Am. Chem. Soc.* **119**, 11910-11919 (1997).